ADVANCED FUNCTIONAL MATERIALS
www.afm-journal.de

# Full-Spectrum Solar Harvesting and Desalination Enabled by Supra-Nano Amorphous Ruthenium Dioxide – Mineral Composites

*Yunchen Long, Zhengyi Mao, Bowen Li, Xiujuan Hu, Xinxue Tang, Yuanchao Liu, Jia-Hua Liu, Hongkun Li, Chong Wang, Hong Yue, Weihui Ou,* Johnny Chung Yin Ho,* Jian Lu,* and Yang Yang Li**

**Breaking crystalline symmetry reveals new photonic capabilities for solar-driven technologies. Herein, a mineral-based supra-nano amorphous ruthenium dioxide composite (a-$Ru_{0.5}$-AM) is constructed. Benefiting from a defect-mediated photon-capturing mechanism in amorphous ruthenium dioxide, a-$Ru_{0.5}$-AM effectively overcomes the near-infrared absorption limitations of rutile-phase ruthenium dioxide (r-Ru), achieving an average absorption of 97% over the entire solar spectrum. Meanwhile, under one sun illumination, a-$Ru_{0.5}$-AM reaches a mean steady-state temperature of 87.91 ± 0.32 °C, and exhibits a thermal buffering effect conducive to efficient thermal confinement. In addition, surface functionalization significantly enhances the utilization efficiency of ruthenium—at equivalent Ru content, the bulk volume of a-$Ru_{0.5}$-AM is ≈10 times larger than that of r-Ru. The integrated a-$Ru_{0.5}$-AM evaporator shows an evaporation rate of 3.37 kg $m^{-2}$ $h^{-1}$ under one sun, with a photothermal conversion efficiency of 97.54%, while showing excellent salt-resistance, long-term stability, multifunctional water purification capability, and outstanding biocompatibility, making it suitable for diverse applications, including ecologically sensitive areas. Overall, this study endows conventional Ru-based materials with novel photothermal functions through defect engineering and surface functionalization, providing a new material design strategy and theoretical basis for applying platinum-group metals in solar steam generation, seawater desalination, and other clean water technologies.**

## 1. Introduction

Driven by the growing urgency for sustainable solar-driven desalination technologies, the development of photothermal materials capable of efficiently harvesting the full solar spectrum has emerged as a key research focus. In recent decades, researchers have extensively explored various photothermal conversion mechanisms to improve solar energy conversion efficiency,[1–5] including localized surface plasmon resonance heating in metallic nanoparticles,[6,7] non-radiative relaxation of photoexcited carriers in semiconductors,[8,9] and vibrational coupling in molecular systems.[10,11] Despite significant advances in surface engineering[12,13] and bandgap tuning strategies,[14,15] most solar-harvesting systems remain intrinsically restricted to the ultraviolet–visible spectral range. This limitation leads to inefficient utilization of incident radiation, leaving substantial portions of the solar spectrum underutilized, particularly in the near-infrared. Therefore, advanced materials capable of

Y. Long, Z. Mao, B. Li, X. Tang, Y. Liu, J.-H. Liu, H. Li, C. Wang, H. Yue, J. C. Y. Ho, J. Lu, Y. Y. Li
Department of Materials Science and Engineering
City University of Hong Kong
Kowloon, Hong Kong, SAR 999077, China
E-mail: johnnyho@cityu.edu.hk; jianlu@cityu.edu.hk; yangli@cityu.edu.hk

Y. Long, J. Lu
State Key Laboratory of Precious Metal Functional Materials
Kunming 650106, China

The ORCID identification number(s) for the author(s) of this article can be found under https://doi.org/10.1002/adfm.202517313



**DOI: 10.1002/adfm.202517313**

Y. Long, X. Tang, J.-H. Liu, H. Li, C. Wang, H. Yue, Y. Y. Li
Center of Super-Diamond and Advanced Films (COSDAF)
City University of Hong Kong
Kowloon, Hong Kong, SAR 999077, China

Y. Long, Z. Mao, Y. Liu, J. Lu, Y. Y. Li
Centre for Advanced Structural Materials
City University of Hong Kong Shenzhen Research Institute
Greater Bay Joint Division
Shenyang National Laboratory for Materials Science
Shenzhen 518057, China

Z. Mao, Y. Liu, J. Lu
Department of Mechanical Engineering
City University of Hong Kong
Kowloon, Hong Kong, SAR 999077, China

ultra-broadband photon harvesting and precise energy localization are urgently needed.

Among the reported photothermal nanomaterials, nanostructures based on gold (Au) and certain platinum-group metals (PGMs) have garnered significant attention in solar-driven seawater desalination owing to their localized surface plasmon resonance (LSPR) effects.[16–19] These materials rely on LSPR to achieve efficient localized photothermal conversion, thereby markedly enhancing evaporation efficiency. However, their photothermal performance is highly dependent on their size and morphology, and their plasmon resonance bandwidths are typically narrow, leading to limited spectral matching with sunlight.[20–22] Although tuning size and morphology or integrating with broadband absorbers such as carbon materials, polymers, and semiconductors can broaden the spectral response and enhance photothermal performance, the complex fabrication processes and high costs still hinder large-scale applications. Consequently, developing alternative materials that combine excellent photothermal performance, broad-spectrum absorption capability, and economic feasibility has become a research focus. Against this backdrop, ruthenium (Ru) has attracted widespread attention in fields such as electrocatalysis,[23,24] photocatalysis,[25,26] supercapacitors,[27,28] and photothermal therapy,[29–31] owing to its relatively lower cost compared with Au and other PGMs (Table S1, Supporting Information) and outstanding optoelectronic and photothermal properties in both elemental and oxide forms. Rutile-phase ruthenium dioxide (r-$RuO_2$) is a gapless semimetal conductor with unique optical response characteristics. However, its rigid band structure limits adaptability to a wide range of photon energies, thereby constraining its potential for broadband photothermal conversion, particularly in solar-driven seawater desalination. To overcome this limitation, defect engineering—such as heteroatom doping, vacancy introduction, and amorphization—has been demonstrated to effectively modulate the electronic structure and optical properties, broaden spectral absorption range, and enhance photothermal response. For example, Chen et al.[32] transformed conventional $\beta$-$Ta_2O_5$ into an amorphous phase and introduced carbon-based heteroatoms, significantly enhancing solar absorption and photothermal performance via the synergistic effects of structural disorder and heteroatom doping. Compared with their crystalline structures, amorphous materials feature disordered atomic arrangements and unsaturated coordination environments, which offer greater flexibility and tunability in optical responses, thus creating new opportunities for light–matter interactions.

Supra-nano materials (<10 nm) have emerged as promising candidates in energy catalysis,[33,34] biomedical applications,[35,36] and electronic devices[37] due to their short ion diffusion paths, abundant active sites, and superior electrochemical properties. Compared with conventional nanomaterials, supra-nano structures exhibit higher atomic utilization efficiency, contributing to enhanced performance and effectively reducing material costs, further expanding their application potential. Among various applications, solar-driven water evaporation is an important area where supra-nano materials showcase their highly efficient photothermal conversion capabilities. However, supra-nano materials typically suffer from high surface energy and thermodynamic instability, making them prone to aggregation, migration, and morphological changes, ultimately leading to performance degradation and structural failure.[38] In recent years, various efficient photothermal systems have been developed for solar-driven water evaporation through the stable dispersion of supra-nanomaterials. For example, Li et al.[16] reported a catalytic evaporator loaded with reduced graphene oxide (rGO)-supported palladium nanoparticles (2.4 nm), which efficiently produces freshwater, salt crystals, and catalytic chemicals simultaneously by synergistically enhancing solar-driven interfacial evaporation and catalytic reactions. Zhu et al.[39] incorporated palladium nanoparticles (5 nm) into natural wood substrates via an impregnation–thermal reduction strategy to fabricate low-cost and highly efficient photothermal evaporators. Therefore, developing effective strategies to stabilize supra-nano structures, suppress aggregation, and maintain excellent performance has become a key challenge in designing advanced photothermal materials.

In this study, an alkali-driven strategy is proposed for the in situ construction of supra-nano amorphous ruthenium dioxide (a-Ru) on an amorphous magnesium-doped calcium carbonate/phosphate mineral scaffold (AM), forming a photothermal network of a-Ru particles with an average diameter of ≈1.70 nm. The resulting composite is denoted as "a-$Ru_x$-AM", where x represents the amount of $Ru^{3+}$ precursor added in millimoles. The a-$Ru_{0.5}$-AM exhibits an average solar absorption of 97%, marking a 5.08% enhancement over rutile-phase ruthenium dioxide (r-Ru). This remarkable enhancement in optical performance is primarily attributed to the atomic-scale disorder within a-Ru and the formation of water-coordinated structural defects, which collectively give rise to novel photon-responsive behaviors distinct from those of crystalline materials. Density functional theory (DFT) calculations indicate that the localized atomic disorder in a-Ru leads to band broadening and the formation of flat electronic states near the Fermi level. These electronic states introduce a higher density of allowed states, effectively enhancing light absorption efficiency. Furthermore, the introduction of defect states reduces the thermal conductivity of ruthenium dioxide, further strengthening energy localization. Notably, this supra-nano design significantly improves material utilization and reduces the overall consumption of the platinum-group metal ruthenium. The a-$Ru_x$-AM-based solar evaporator delivers excellent water evaporation performance and remarkable operational stability under practical conditions, highlighting its promising prospects for efficient and stable solar-driven photothermal water treatment applications.

W. Ou
School of Chemical Engineering and Light Industry
Guangdong University of Technology
Guangzhou 510006, China
E-mail: weihuiou@gdut.edu.cn
X. Hu
Department of Physics
City University of Hong Kong
Kowloon, Hong Kong, SAR 999077, China

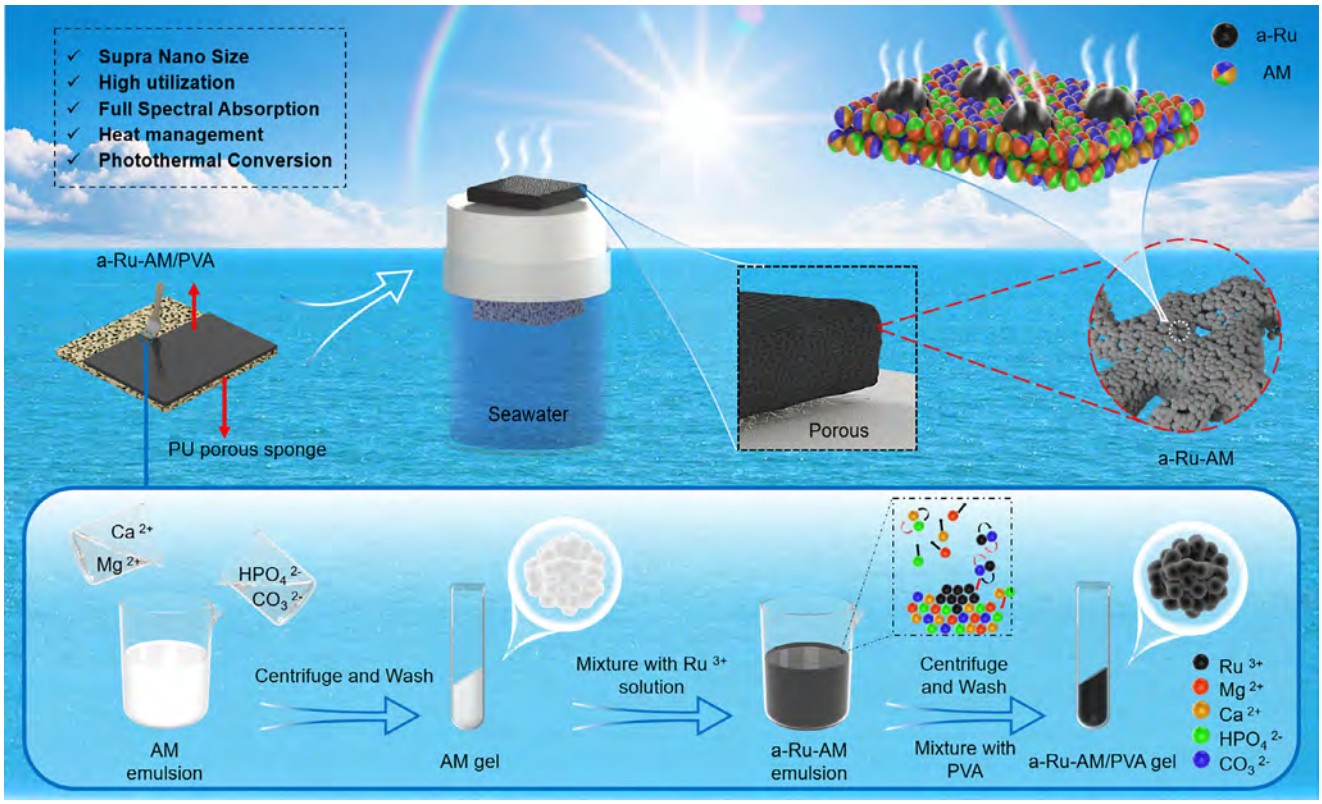


**Figure 1.** Schematic illustration of the synthesis route and solar-driven desalination application of a-Ru-AM.

## 2. Results and Discussion

### 2.1. Structural and Compositional Characterization

Herein, a simple and efficient solution-based synthesis strategy was employed to construct a mineral-based supra-nano amorphous ruthenium dioxide composite (a-Ru-AM). The overall synthesis route of a-Ru-AM and its integration into a solar evaporator device are illustrated in **Figure 1**. The amorphous mineral scaffold is based on the Mg-doped amorphous calcium carbonate/phosphate composite (denoted as "AM") synthesized in our previous study,[40,41] which exhibits long-term phase stability and nanoscale particle size. Specifically, aqueous solutions of $Ca^{2+}$, $Mg^{2+}$, $CO_3^{2-}$, and $HPO_4^{2-}$ were mixed in stoichiometric ratios and thoroughly stirred, followed by centrifugation to obtain a milky-white AM precipitate. The resulting AM material demonstrates excellent dispersibility in aqueous solution (Figure S1a,b, Supporting Information). Subsequently, a $RuCl_3$ solution with a predetermined concentration was rapidly added to the AM dispersion. The molar amount of $Ru^{3+}$ is denoted as x, and the resulting composite is referred to as a-$Ru_x$-AM. Upon introduction of $Ru^{3+}$, the suspension rapidly changed color from milky-white to uniform gray-black, and maintained good dispersion stability in water (Figure S1c, Supporting Information). This pronounced and uniform color change indicated rapid and effective deposition of $Ru^{3+}$ onto the scaffold. After further centrifugation, the resulting supernatant appeared nearly transparent—comparable to pure water, suggesting that most of the $Ru^{3+}$ had been adsorbed and immobilized by the mineral scaffold. Inductively coupled plasma optical emission spectroscopy (ICP-OES) further confirmed the near-complete removal of $Ru^{3+}$ from the solution (Figures S1d and S2, Supporting Information). These results reveal strong interfacial interactions between AM and $Ru^{3+}$, driven primarily by a synergistic mechanism involving interfacial ionic immobilization and hydrolysis-induced coprecipitation. This process facilitates in situ formation and spatial confinement of supra-nano a-Ru within the AM scaffold.

To investigate the effect of $Ru^{3+}$ concentration on the morphological and structural evolution of the composite materials, a series of samples was systematically characterized by scanning electron microscopy (SEM). Preliminary observations revealed that the pristine AM material exhibited a uniform granular morphology and a white appearance (**Figure 2a**, Inset). At lower $Ru^{3+}$ loadings, both a-$Ru_{0.1}$-AM and a-$Ru_{0.5}$-AM retained a particulate structure similar to pristine AM (Figure 2b,c). At a higher $Ru^{3+}$ concentration of 1 mmol, the a-$Ru_1$-AM sample displayed marked morphological changes, characterized by the coexistence of microscale agglomerates and granular domains (Figure 2d). In addition to morphological evolution, a-$Ru_x$-AM exhibited progressive color changes with increasing $Ru^{3+}$ concentration. At 0.5 mmol, the a-$Ru_{0.5}$-AM reached visual color saturation, and further increase to 1 mmol produced negligible additional color change (Figure 2b–d, Inset). Energy-dispersive X-ray spectroscopy (EDS) analysis indicated that these block-like agglomerates were enriched in Ca and P (Figure S3a,b, Supporting Information). Further microstructural analysis by

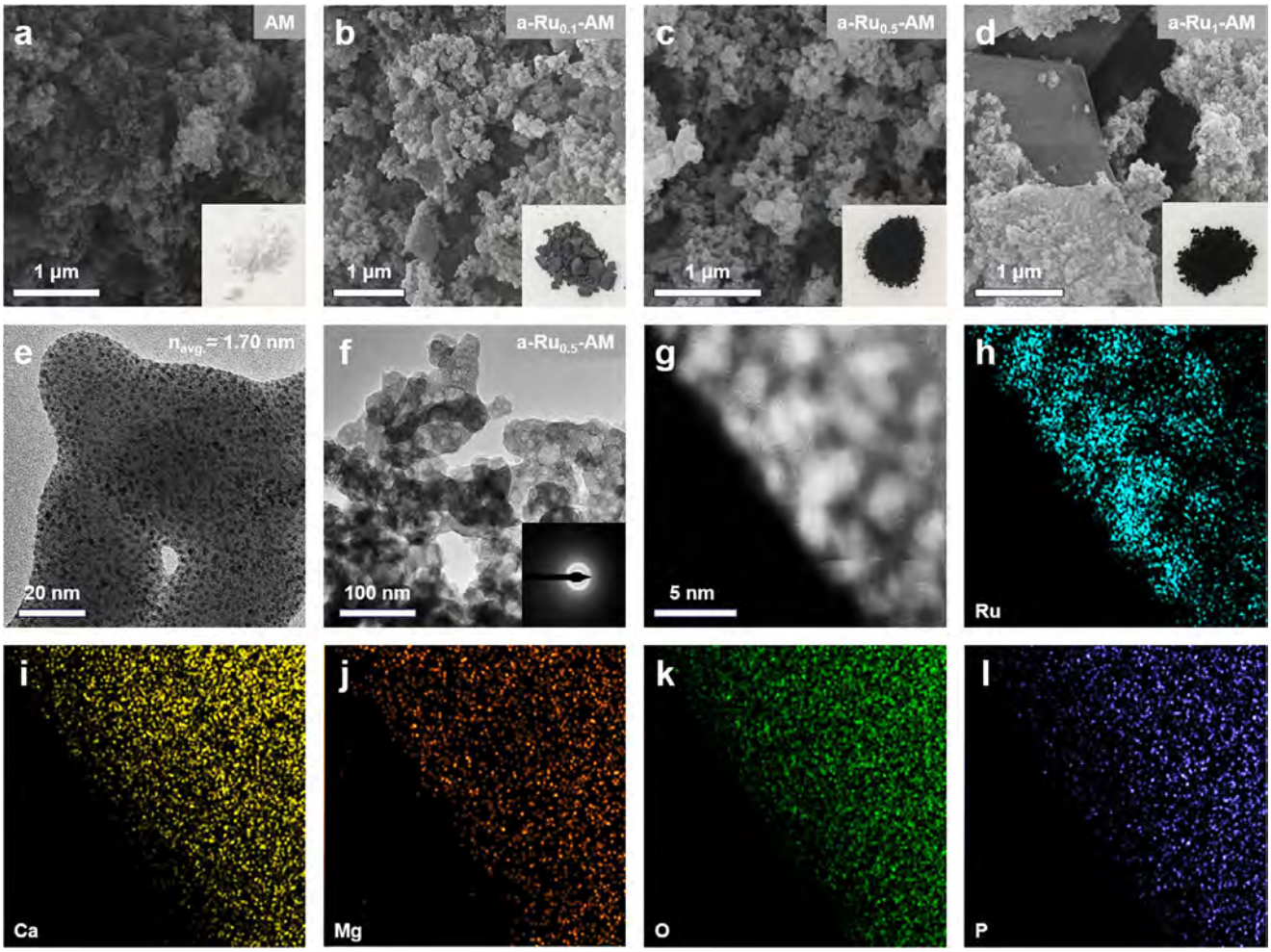


**Figure 2.** Morphological and structural characterization of a-Ru-AM. a–d) Scanning electron microscopy (SEM) images of a-$Ru_x$-AM with varying Ru content (x = 0, 0.1, 0.5, 1 mmol). Insets: corresponding digital photographs. e,f) High-resolution transmission electron microscopy (HRTEM) images of a-$Ru_{0.5}$-AM. Inset: selected-area electron diffraction (SAED) patterns. g–l) High-angle annular dark-field scanning transmission electron microscopy (HAADF-STEM) images of a-$Ru_{0.5}$-AM and corresponding energy-dispersive X-ray spectroscopy (EDS) elemental maps of Ru, Ca, Mg, O, and P.

high-resolution transmission electron microscopy (HRTEM) revealed uniformly distributed quasi-spherical particles, 1–2.5 nm in diameter, on the surface of a-$Ru_{0.5}$-AM (Figure 2e; Figure S4, Supporting Information). With an average diameter of ≈1.7 nm, these particles fall within the supra-nano size regime. Selected area electron diffraction (SAED) patterns showed no discernible diffraction rings (Figure 2f, Inset), further confirming their amorphous character.[42] Consistent with the SAED results, high-angle annular dark-field scanning transmission electron microscopy (HAADF-STEM) imaging (Figure S5a,b, Supporting Information) revealed no detectable lattice fringes, further affirming the amorphous character of the formed a-Ru species. Elemental mapping by EDS (Figure 2g–l) showed that Ru was enriched in the supra-nano domains, while Ca, Mg, O, and P were uniformly distributed across the AM scaffold. Further spatial elemental analysis (Figure S5c,d, Supporting Information) confirmed the homogeneous dispersion of Ru across the composite scaffold. These results demonstrate that the employed synthesis strategy effectively achieved uniform supra-nano a-Ru loading.

X-ray diffraction (XRD) analysis revealed a marked effect of $Ru^{3+}$ concentration on the phase structure of the mineral gel-based composites (**Figure 3**a). At $Ru^{3+}$ concentration ≤ 0.5 mmol (i.e., a-$Ru_{0.1}$-AM to a-$Ru_{0.5}$-AM), the resulting materials maintained an amorphous feature similar to the pristine AM, with no apparent crystalline diffraction peaks observed. This result aligns well with the absence of diffraction rings observed in TEM, further confirming the amorphous dispersion of a-Ru on the AM scaffold surface. This amorphous structure is attributed to the rapid hydrolytic deposition of $Ru^{3+}$ under alkaline conditions, a reaction pathway that favors the formation of amorphous ruthenium oxides rather than crystalline phases. Upon increasing the $Ru^{3+}$ concentration to 1 mmol (a-$Ru_1$-AM), distinct crystalline diffraction peaks emerged in the XRD pattern. These peaks can be indexed to $CaHPO_4{\cdot}2H_2O$ crystals (PDF#72-0713). This observation is consistent with the EDS findings, which identified Ca and P as the main constituents of the microscale block-like aggregates.

To gain deeper insights into the nucleation mechanism of a-Ru, dynamic changes in ionic species during the reaction were

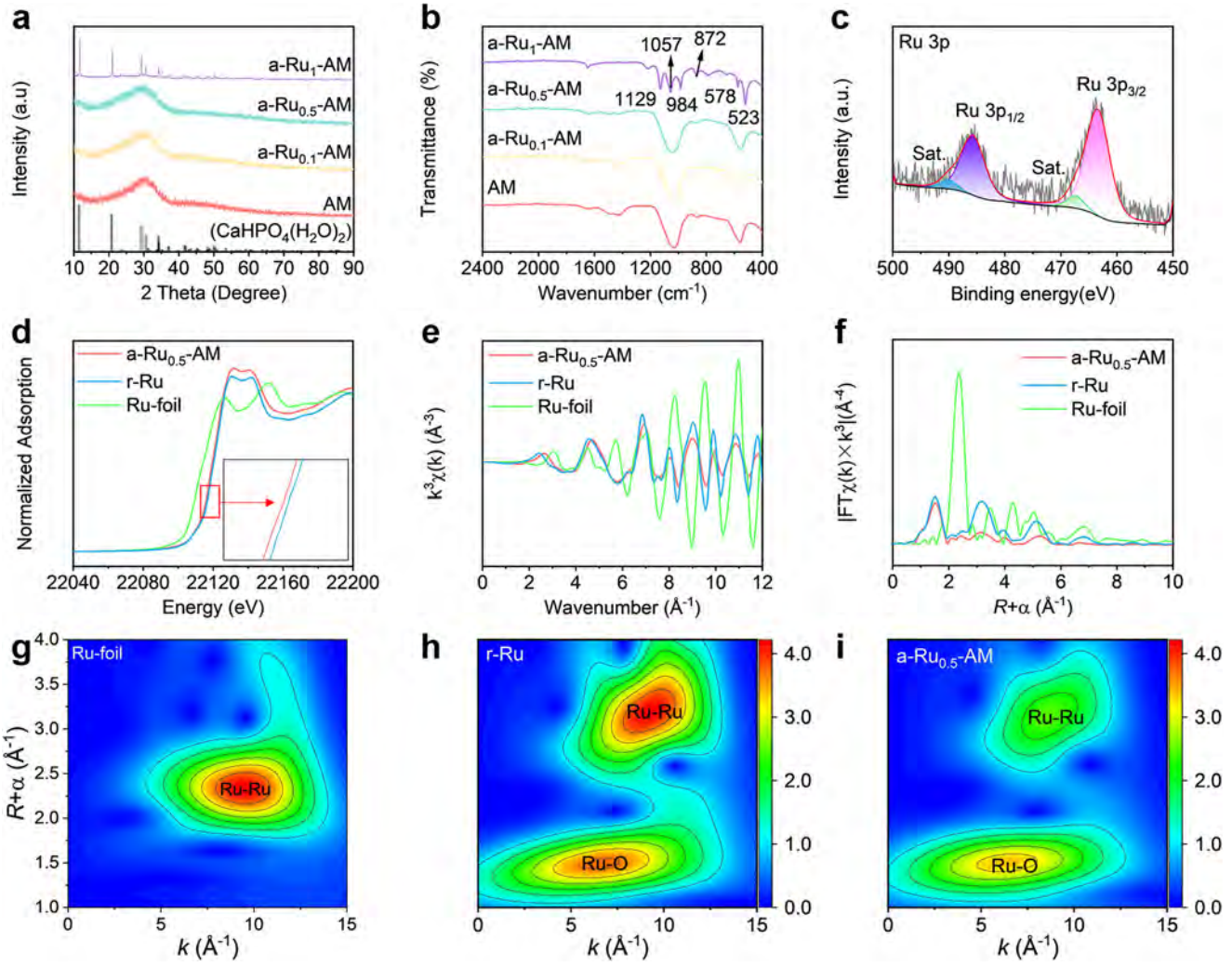


**Figure 3.** Structural and chemical characterization of a-Ru-AM: a) X-ray diffraction (XRD) patterns, and b) Fourier transform infrared (FTIR) spectra of a-Ru$_x$-AM and AM. c) High-resolution X-ray photoelectron spectroscopy (XPS) Ru 3p core-level spectrum of a-Ru$_{0.5}$-AM. d) Normalized Ru *K*-edge X-ray absorption near edge structure (XANES) spectra. e) *K*-edge extended XANES oscillation functions $k^3\chi(k)$. f) $k^3$-weighted Fourier-transformed extended X-ray absorption fine structure (FT-EXAFS) Ru *K*-edge spectra. g–i) Wavelet transform (WT)-EXAFS plots of Ru *K*-edge of Ru-foil, r-Ru, a-Ru$_{0.5}$-AM.

monitored via solution-phase ion analysis. The results suggest that the reaction proceeds via a multi-ion release pathway. As the $Ru^{3+}$ loading on the AM scaffold increased, the concentrations of $Ca^{2+}$ and $Mg^{2+}$ in the supernatant also rose accordingly (Figure S6, Supporting Information). This observation implies a $CO_3^{2-}$-mediated cascade reaction mechanism. Specifically, $Ru^{3+}$ undergoes oxidation under alkaline conditions to form a-Ru, which concurrently consumes the carbonate matrix. This disrupts the local structural stability of the AM scaffold, leading to the release of $Ca^{2+}$, $Mg^{2+}$, and $HPO_4^{2}$. Subsequently, the released $Ca^{2+}$ reacts with $HPO_4^{2-}$ to generate the byproduct $CaHPO_4{\cdot}2H_2O$. This reaction pathway is corroborated by characteristic vibrational bands observed in the Fourier transform infrared (FTIR) spectra (Figure 3b).[43] Simultaneously, thermogravimetric analysis (Figure S7, Supporting Information) shows a distinct mass loss in the range of 450–500 °C, which is attributed to the thermal decomposition of $CaHPO_4{\cdot}2H_2O$ into pyrophosphate, consistent with known phase transformation processes reported in the literature.[44] Moreover, a stoichiometric correlation was observed between $Ru^{3+}$ addition and the leaching of $Ca^{2+}/Mg^{2+}$, indicating that the formation of a-Ru is closely related to the decalcification of the matrix. Specifically, $Ru^{3+}$ undergoes spontaneous nucleation and localized deposition at the AM/$RuCl_3$ interface through the consumption of $CO_3^{2-}$, ultimately forming a supranano amorphous surface-bound structure.

To further clarify the chemical states and bonding environments of the elements in a-Ru$_{0.5}$-AM, high-resolution X-ray photoelectron spectroscopy (XPS) analysis was performed. The full XPS survey spectrum (Figure S8a, Supporting Information) indicates the presence of Ru, Ca, Mg, O, and P, confirming the basic elemental composition of the composite. High-resolution Ru 3p spectra (Figure 3c) show two distinct peaks at binding energies of 463.81 and 485.89 eV, corresponding to the $3p_{3/2}$ and $3p_{1/2}$ orbitals, respectively. These values indicate the $Ru^{4+}$ oxidation state, confirming that ruthenium is incorporated into the composite in a stable oxidized form.[45] In addition to the Ru 3p

signals, the deconvoluted C 1s spectrum, which partially overlaps with the Ru 3d region, exhibits a distinct peak at 281.72 eV, further supporting the presence of $Ru^{4+}$ (Figure S8b, Supporting Information).[46] Additionally, high-resolution spectra of Ca 2p and Mg 1s (Figure S8c,d, Supporting Information) indicate that both framework cations retain their original oxidation states post-doping, with no discernible shifts in binding energy. These findings suggest that the $Ru^{3+}$ doping process does not compromise the chemical stability of the mineral matrix, thereby preserving its structural and functional integrity for subsequent photothermal applications.

Synchrotron-based X-ray absorption spectroscopy was employed to investigate the electronic structure and local coordination environment of Ru species in a-$Ru_{0.5}$-AM via Ru *K*-edge X-ray absorption near-edge structure (XANES) and extended X-ray absorption fine structure (EXAFS) analyses. Metallic Ru foil and commercial r-Ru were used as reference materials to establish benchmarks for oxidation state and structural comparison. The Ru *K*-edge XANES spectra (Figure 3d) reveal that the absorption edge of a-$Ru_{0.5}$-AM lies between that of metallic Ru and r-Ru, yet closer to r-Ru, indicating a Ru oxidation state close to +4 and the absence of metallic features. Notably, the absorption edge of a-$Ru_{0.5}$-AM is slightly shifted to lower energy relative to r-Ru, suggesting a marginally lower average oxidation state than +4.[47,48] The $k^3$-weighted EXAFS oscillation profile of a-$Ru_{0.5}$-AM resembles that of r-Ru, implying a comparable local coordination environment. However, the markedly attenuated oscillation amplitude indicates higher structural disorder and a higher density of under-coordinated sites in a-$Ru_{0.5}$-AM (Figure 3e).[49] Further Fourier-transformed EXAFS (FT-EXAFS) analysis reveals prominent coordination peaks at ≈1.5 Å (Ru–O) and ≈3.1 Å (Ru–Ru), consistent with the typical rutile structure of r-Ru. However, the reduced peak intensities indicate a lower coordination number (Figure 3f).[50] Quantitative fitting reveals that the average Ru–O coordination number in a-$Ru_{0.5}$-AM is 4.7, significantly lower than the value of 6 in r-Ru. This result further confirms the amorphous nature and structural defects of a-$Ru_{0.5}$-AM, likely arising from disordered atomic arrangements and coordinated water molecules (Figure S9 and Table S2, Supporting Information). Wavelet transform EXAFS (WT-EXAFS) analysis provides spatial – *k*-space resolution of different scattering paths, confirming the simultaneous presence of Ru–O (6.5 $Å^{-1}$) and Ru–Ru (9 $Å^{-1}$) coordination in a-$Ru_{0.5}$-AM. No signals indicative of metallic Ru aggregation were detected (Figure 3g–i). These findings are consistent with the aforementioned $k^3$-weighted EXAFS and FT-EXAFS results, further confirming the highly defective amorphous Ru species in a-$Ru_{0.5}$-AM. Such structural features provide a critical foundation for its exceptional photothermal performance.

### 2.2. Light Harvesting and Photothermal Conversion

Amorphous materials, due to their disordered atomic arrangements and continuously distributed electronic density of states, offer distinct advantages in spectral response, facilitating efficient absorption of broadband solar radiation. To systematically evaluate the solar energy harvesting performance of the a-$Ru_x$-AM composites, we investigated their light absorption behavior by varying the a-Ru loading content. As shown in the UV–vis–NIR absorption spectra, the absorption rate of a-$Ru_x$-AM increased with the a-Ru content (Figure S10, Supporting Information). Once the a-Ru concentration reached 0.5 mmol, the system exhibited absorption saturation, as indicated by the nearly identical spectra of a-$Ru_{0.5}$-AM and a-$Ru_1$-AM, showing 97% and 96.88% absorption efficiencies, respectively. To further quantify the photothermal conversion performance, equal masses (0.1 g) of a-$Ru_{0.5}$-AM and a reference sample of r-Ru (prepared via thermal decomposition) were irradiated under simulated solar light (1.0 kW $m^{-2}$), with real-time surface temperature monitoring. XRD and SEM confirmed the phase and morphology of the r-Ru sample to ensure comparability (Figure S11, Supporting Information). As shown in **Figure 4**a, a-$Ru_{0.5}$-AM exhibited a rapid temperature rise to 84.01 ± 1.48 °C within 180 s and stabilized at 87.91 ± 0.32 °C after 380 s (Video S1, Supporting Information). Thermal relaxation tests showed that the system returned to the ambient temperature within 360 s after turning off the light source. Notably, the steady-state temperature of a-$Ru_{0.5}$-AM was significantly higher than that of r-Ru (81.65 ± 0.91 °C), clearly demonstrating the superior solar-to-thermal conversion efficiency of the a-$Ru_{0.5}$-AM (Figure 4b; Table S3 and Video S2, Supporting Information). Moreover, the heating and cooling processes of a-$Ru_{0.5}$-AM were slower than those of r-Ru, suggesting enhanced thermal buffering kinetics. This behavior was further corroborated by thermal conductivity measurements (Figure S12, Supporting Information), which confirmed the excellent thermal buffering capacity of the composite. This slow-release thermal behavior is particularly critical for sustained evaporation under intermittent solar conditions (e.g., nighttime or cloudy weather), as it helps maintain a localized thermal field and enables all-day solar-driven desalination. Such a property is essential for the development of stable and reliable water purification systems.

To elucidate the role of crystal symmetry breaking in modulating the anomalous optical behavior of ruthenium dioxide, we systematically compared the structure–property relationships of a-Ru and r-Ru. This comparison confirmed the critical contribution of the a-Ru component to the enhanced photothermal performance of a-$Ru_{0.5}$-AM. First-principles density functional theory (DFT) calculations were performed to construct atomic models of a-Ru (Figure 4c) and r-Ru (Figure S13, Supporting Information), and to predict their optical responses. The results revealed that a-Ru exhibits a comparatively flat refractive index (*n*) profile across the entire solar spectrum, with significantly lower n values in the near-infrared (NIR) region compared to r-Ru (Figure S14a, Supporting Information). This behavior can be attributed to the atomic disorder and defect-induced redistribution of local electronic states in the amorphous structure. In contrast, r-Ru exhibits a higher extinction coefficient (*k*) due to its long-range periodicity, which can be ascribed to enhanced photon attenuation (Figure S14b,c, Supporting Information). Although higher *k* values suggest that the crystalline phase possesses stronger broadband absorption, according to the Fresnel equation, reflectance $R = \frac{(n-1)^2+k^2}{(n+1)^2+k^2}$, the reflectance is governed by both *k* and *n*. The lower and uniform n values of a-Ru across the solar spectrum help suppress reflection losses, synergistically enhancing solar absorption over a broad wavelength range. To eliminate potential interference from the AM framework and particle size effects on optical measurements, we synthesized compositionally

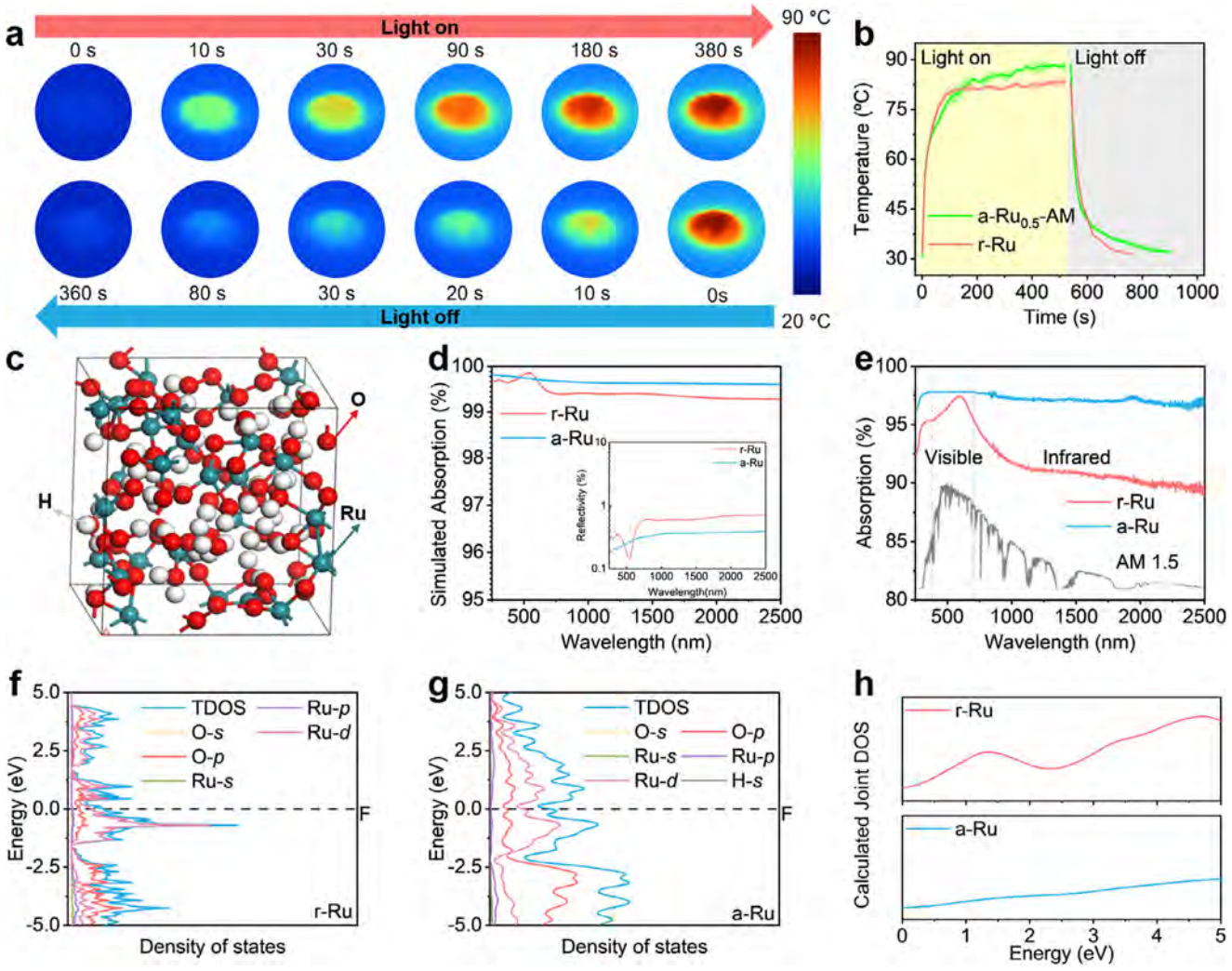


**Figure 4.** Photothermal conversion performance and theoretical mechanism of a-Ru-AM: a) Infrared thermal images of a-$Ru_{0.5}$-AM under one sun illumination. b) Time-dependent surface temperature profiles of a-$Ru_{0.5}$-AM, and r-Ru under one sun illumination, followed by cooling after light off. c) Optimized atomic structure model of a-Ru. d) Simulated optical absorption spectra of a-Ru and r-Ru. e) Experimental absorption spectra of a-Ru and r-Ru. f,g) Total and partial density of states of r-Ru and a-Ru. h) Joint density of states for r-Ru and a-Ru.

pure a-Ru samples free of the AM framework for direct comparison with r-Ru. The a-Ru samples were prepared via an identical alkaline solution-based method, and XRD and SEM verified their phase and morphology to ensure comparability between the two systems (Figure S15, Supporting Information). As shown in Figure 4d,e, the UV–vis–NIR spectra obtained from both experimental measurements and theoretical simulations exhibit consistent variations between r-Ru and a-Ru. These results clearly demonstrate that crystal symmetry breaking is pivotal to enabling broadband solar absorption in a-Ru, particularly in enhancing the near-infrared (780–2500 nm) response.

A deeper understanding of the origin of a-Ru's superior optical properties was achieved through density functional theory (DFT) simulations, which unveiled the evolution of its electronic structure. As shown in Figure 4f and Figure S16a (Supporting Information), r-Ru exhibits a significant overlap between the conduction and valence bands near the Fermi level, indicating a pronounced metallic character. The Ru 4d orbitals dominate the region around the Fermi level due to localized d–d electronic interactions, forming a high density of states (DOS). This localized electronic distribution accounts for the strong visible-light absorption observed in r-Ru and aligns with its high extinction coefficient ($k$).[51] Moreover, prominent DOS peaks in the visible range further support its excellent photon-harvesting capability. In contrast, a-Ru features a disordered atomic structure, and while its DOS near the Fermi level remains continuously distributed, indicating metallic behavior (Figure 4g; Figure S16b, Supporting Information), the absence of long-range order results in electron delocalization. This leads to broadening of the total density of states (TDOS) peaks compared to r-Ru. Notably, defect-induced states near the Fermi level introduce numerous flat bands, thereby extending the spectral absorption window and significantly enhancing the broadband optical response of a-Ru.[32,52] Joint density of states (JDOS) analysis further reveals the fundamental difference between the two materials (Figure 4h). r-Ru, with its crystalline long-range order,

exhibits narrow and intense JDOS peaks, indicating that its optical transitions are concentrated in specific wavelength regions. In contrast, a-Ru displays a broader, lower-intensity JDOS profile extending into the near- and mid-infrared regions. This broadening arises from defect states that fill the bandgap region, suggesting a more uniform and broadband light absorption capability in the amorphous structure. This JDOS reconstruction highlights the advantage of a-Ru over its crystalline counterpart in full-spectrum energy management. Meanwhile, experimental observations showed that a-Ru exhibited a higher steady-state temperature than r-Ru, along with a pronounced photothermal response delay, and a thermal buffering effect, indicating that the atomic disorder has enhanced the full-spectrum energy management capability of a-Ru (Figure S17, Supporting Information). In summary, the exceptional photothermal performance of the a-$Ru_{0.5}$-AM composite primarily originates from the supra-nano a-Ru domains functionalized on the mineral gel framework. The synergistic effects of atomic-level disorder and supra-nano size enhance light absorption and facilitate efficient photothermal conversion.

### 2.3. Solar-Driven Desalination Application

The practical utility of a-$Ru_{0.5}$-AM was further demonstrated by integrating it as the core photothermal component in a solar-driven water evaporation system. The a-$Ru_{0.5}$-AM evaporation layer was prepared as follows: First, a-$Ru_{0.5}$-AM was embedded into a polyvinyl alcohol (PVA) hydrogel matrix, with sodium chloride (NaCl) serving as a templating agent to form a composite mixture. This composite mixture was then coated onto the surface of a commercial polyurethane foam substrate. Subsequently, a series of treatments, including freeze-drying, liquid nitrogen quenching, and salt leaching, was performed to obtain a porous composite structure. Additionally, an insulating layer was introduced at the bottom of the evaporator to minimize heat loss and enhance localized heat concentration. Meanwhile, the overall geometry of the water supply layer was optimized to reduce thermal dissipation (Figure S18, Supporting Information). Optical characterization confirmed that a-$Ru_{0.5}$-AM exhibits broadband solar absorption comparable to that of state-of-the-art carbon-based materials, including graphene and carbon nanotubes. Benefiting from the excellent dispersibility of a-$Ru_{0.5}$-AM within the PVA hydrogel matrix, along with the rough surface texture and interconnected porous network of the composite hydrogel, the a-$Ru_{0.5}$-AM evaporator achieved a high solar absorptance of 97.61% (**Figure** 5a; Figure S19, Supporting Information), along with excellent hydrophilicity and water permeability (Figure S20, Supporting Information)—both essential for efficient photothermal evaporation. The evaporator exhibited rapid and strong localized heating under one sun illumination (1.0 kW $m^{-2}$), with the surface temperature reaching 38.18 °C within 5 min and stabilizing at 41.36 °C after 10 min, while the bulk water temperature remained nearly unchanged (Figure 5b; Figures S21 and S22, Supporting Information). This localized thermal field drove the water loss mass of 3.37 kg $m^{-2}$, corresponding to a photothermal conversion efficiency of 97.54% (Figure 5c). This performance significantly exceeds that of pure water (0.58 kg $m^{-2}$), AM (1.29 kg $m^{-2}$), and r-Ru (2.81 kg $m^{-2}$), by factors of 5.81, 2.61, and 1.20, respectively. Notably, the hydrogel composite matrix also contributed to a substantial reduction in the evaporation enthalpy of water. This reduction is attributed to interfacial interactions between water molecules and the PVA polymer network, which facilitate the release of bound water with lower energy input (Figure S23, Supporting Information). To optimize the evaporator's performance, a series of tests was conducted by varying the a-$Ru_{0.5}$-AM powder content within the PVA hydrogel from 2.5 to 10 wt.%. As shown in Figure 5d, increasing the loading from 2.5 to 10 wt.% resulted in a corresponding rise in evaporation rate from 3.15 to 3.37 kg $m^{-2}$ $h^{-1}$—consistently outperforming the 5 wt.% a-Ru and r-Ru controls. The optimal evaporation rate was observed at a 5 wt.% loading of a-$Ru_{0.5}$-AM, which was subsequently selected for both indoor and outdoor water collection tests.

The a-$Ru_{0.5}$-AM evaporator exhibited excellent durability under practical operating conditions. During continuous operation in natural seawater (sourced from Victoria Harbour, Hong Kong) for 40 h, the device maintained a stable average evaporation rate of 3.37 kg $m^{-2}$ $h^{-1}$ (Figure 5e), with negligible changes in the phase composition of the photothermal active components before and after use (Figure S24, Supporting Information). In addition to its high operational stability, the a-$Ru_{0.5}$-AM evaporator demonstrated remarkable resistance to salt fouling as well as a self-cleaning capability during overnight operation. Notably, 1 g of pre-deposited NaCl crystals on the evaporator surface completely dissolved within 6 h (Figure 5e, Insets), effectively preventing salt accumulation and ensuring unobstructed evaporation pathways. This anti-scaling behavior ensures sustained evaporation performance and enhances the long-term operational reliability of the system. Even under extreme salinity conditions (20 wt.% NaCl), the a-$Ru_{0.5}$-AM evaporator maintained stable and robust performance. Although a slight decline in evaporation rate was observed—primarily due to reduced water transport caused by mild shrinkage of the PVA hydrogel matrix—salt crystallization was confined to the device's edges after 10 h of continuous operation, with most of the surface remaining clean, demonstrating excellent salt tolerance in high-salinity environments (Figure 5f, Insets). A solar-driven desalination prototype was designed and constructed to assess the system's real-world applicability further. The device featured an effective evaporation area of 80 × 80 $mm^2$ and a photothermal layer thickness of 2 mm (Figure S25a,b, Supporting Information). Outdoor photothermal tests revealed that, compared to a pure PVA-based evaporator, the a-$Ru_{0.5}$-AM evaporator exhibited faster surface temperature rise and earlier condensation of water droplets under natural sunlight (Figure S25b and Videos S3–S6, Supporting Information). Formal outdoor desalination tests were conducted on August 1, 2025, under partly cloudy weather with an average ambient temperature of 30.1 °C (Meteorological data comes from King's Park Weather Station, Hong Kong, Supporting Information S1). Over 8 h of natural sunlight exposure (10:00 a.m. to 6:00 p.m.), the prototype steadily produced 65.52 g of clean water, corresponding to a daily water yield of ≈10.24 kg $m^{-2}$ $day^{-1}$ (Figure S25c,d, Supporting Information). Ion chromatography analysis of the collected water confirmed that the concentrations of principal ions—including $Na^+$, $Mg^{2+}$, $K^+$, and $Ca^{2+}$—were reduced by > 99% (Figure 5g), validating the system's excellent desalination performance and freshwater production efficiency in practical scenarios.

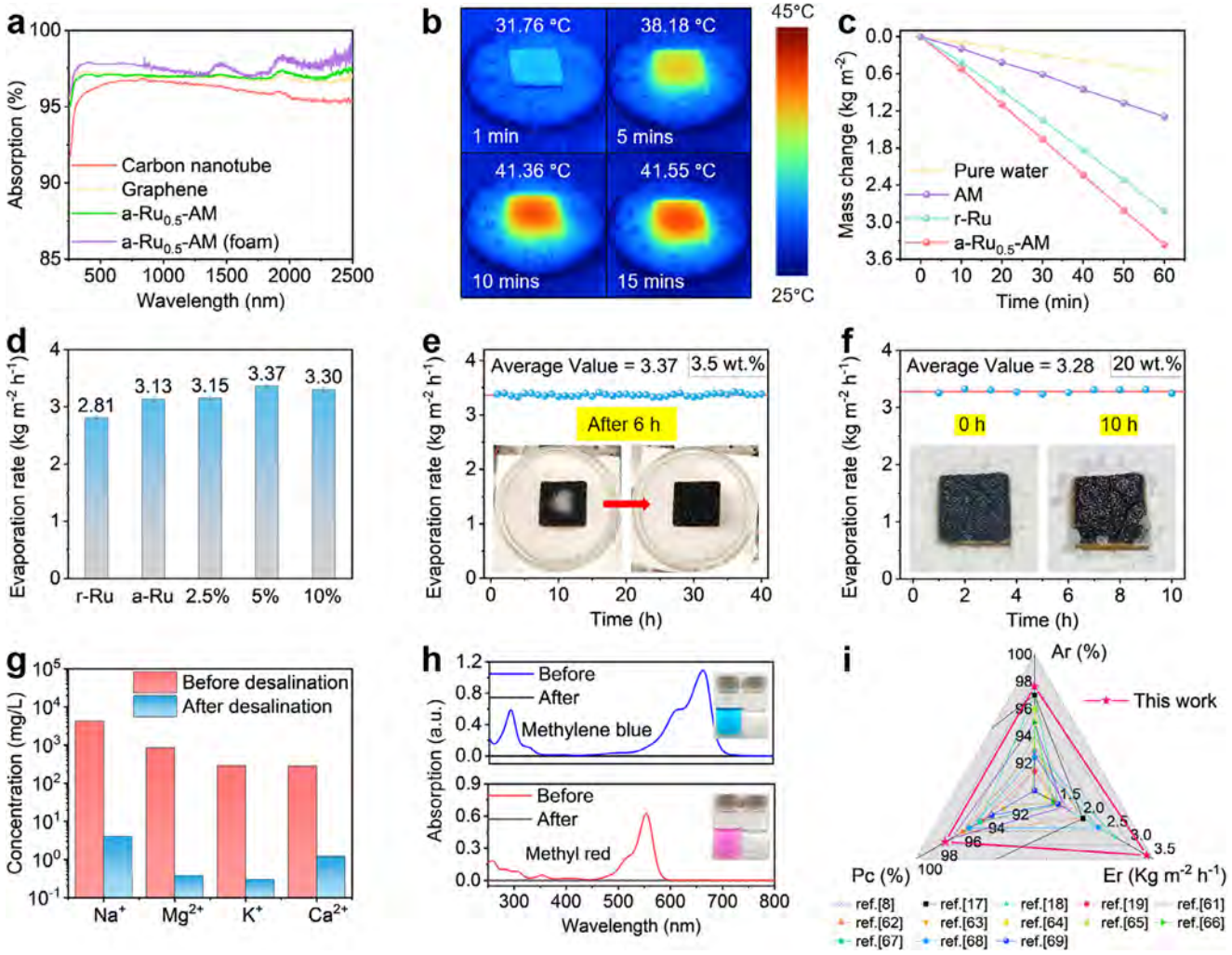


**Figure 5.** Solar-driven desalination and purification performance of a-Ru-AM system: a) Absorption spectra of a-$Ru_{0.5}$-AM gel, a-$Ru_{0.5}$-AM (foam) evaporator, carbon nanotubes, and graphene. b) Infrared thermal images of a-$Ru_{0.5}$-AM evaporator under 1 sun illumination at different time intervals. c) Water mass loss for pure water, AM, 5wt.% r-Ru, and 5wt.% a-$Ru_{0.5}$-AM evaporators under 1 sun. d) Mean evaporation rate of 5 wt.% r-Ru and 5 wt.% a-Ru, and varying filling amounts of a-$Ru_{0.5}$-AM. e) Long-term evaporation in natural seawater. Insets: photograph of salt fouling resistance after preloading salt crystals. f) 10-h evaporation of 20 wt.% brine. Insets: photograph of salt accumulation resistance. g) Metal ion concentrations before and after solar desalination. h) UV–vis–NIR spectra of dye solutions (methylene blue, methyl red) pre- and post-purification. i) Performance comparison with other noble-metal-based systems in absorption rate (Ar), photothermal conversion (Pc), and evaporation rate (Er).

The multifunctionality of the photothermal evaporation system endows it with broad applicability across diverse water purification scenarios.[53–58] Among these, the removal of organic chromophoric contaminants is particularly critical for environmental remediation. In a typical evaporation–condensation cycle, the a-$Ru_{0.5}$-AM evaporator effectively removes organic chromophoric contaminants such as red and blue dyes. UV–vis–NIR spectroscopy reveals that the absorption peaks of the condensed water completely disappeared after treatment, indicating thorough decolorization (Figure 5h). Beyond its decontamination capability, the ecological safety of a-$Ru_{0.5}$-AM was rigorously validated. Biocompatibility tests based on cell viability indicate that a-$Ru_{0.5}$-AM exerts negligible cytotoxicity (Figure S26, Supporting Information), indicating excellent biological inertness and suitability for deployment in ecologically sensitive desalination systems. From both cost-effectiveness and resource utilization perspectives, a-$Ru_{0.5}$-AM offers notable economic advantages. The surface functionalization strategy markedly enhanced Ru utilization efficiency while reducing the total Ru consumption. Volumetric analysis showed that, under the same total mass condition (0.1 g), a-$Ru_{0.5}$-AM occupied approximately four times the bulk volume of pure a-Ru and r-Ru (Figure S27a–c, Supporting Information). Quantitative evaluation further revealed that, for the same Ru content, the total mass of a-$Ru_{0.5}$-AM was 2.9 times that of r-Ru, accompanied by an approximately tenfold increase in bulk volume (Figure S27d, Supporting Information). Notably, at equal total mass loading, the actual Ru content in the a-$Ru_{0.5}$-AM evaporator was substantially lower than in the r-Ru/a-Ru counterpart, yet it delivered superior photothermal evaporation performance (Figure S28, Supporting Information). Consequently, a-$Ru_{0.5}$-AM achieved high photothermal performance while significantly lowering Ru consumption, thereby improving

both utilization efficiency and cost-effectiveness per unit Ru. Furthermore, the a-$Ru_{0.5}$-AM evaporator demonstrates outstanding photothermal responsiveness and energy conversion efficiency, achieving an average absorption of 97.61%, an evaporation rate of 3.37 kg $m^{-2}$ $h^{-1}$, and a photothermal conversion efficiency of 97.54%. Compared to previously reported solar evaporation systems based on gold and other PGMs, the a-$Ru_{0.5}$-AM evaporator exhibits superior comprehensive performance (Figure 5i; Table S4, Supporting Information).[8,17–19,59–67] Collectively, these results indicate that the preparation strategy of a-$Ru_{0.5}$-AM provides a practical and scalable route toward high-performance, low-cost solar water treatment technologies.

## 3. Conclusion

In this work, we propose a defect-mediated strategy to enhance the solar-to-thermal energy conversion performance of ruthenium dioxide. As a proof of concept, we synthesized a mineral-based supra-nano amorphous ruthenium dioxide (a-Ru-AM) photothermal composite. This strategy effectively addresses three key challenges in conventional photothermal material design: 1) overcoming the trade-off between spectral response range and light absorption efficiency, 2) balancing high material performance with economic feasibility, and 3) achieving a coordinated optimization of energy localization and system multifunctionality. Optical characterization combined with density functional theory (DFT) calculations indicates that the a-Ru phase in a-$Ru_{0.5}$-AM introduces defect-induced localized states near the Fermi level due to its disordered structure. This structural disorder generates abundant flat bands that significantly broaden the spectral absorption range, enabling broadband solar absorption of 97% and effectively compensating for the insufficient near-infrared absorption of r-Ru. In addition, the a-$Ru_{0.5}$-AM-based photothermal conversion system can reach and stably maintain a surface temperature of 87.91 ± 0.32 °C under standard one sun illumination, exhibiting excellent photothermal responsiveness and thermal buffering capability. Furthermore, the a-$Ru_{0.5}$-AM evaporator achieves a high evaporation rate of up to 3.37 kg $m^{-2}$ $h^{-1}$ and a photothermal conversion efficiency of 97.54%. By synergistically coupling amorphous structural engineering with natural mineral templating, this work establishes a new paradigm for the functionalization and performance enhancement of Ru-based materials and lays a solid foundation for the broader application of platinum-group metals in sustainable energy fields such as solar-driven seawater desalination and environmental purification.

## Supporting Information

Supporting Information is available from the Wiley Online Library or from the author.

## Acknowledgements

Y.L., Z.M., and B.L. contributed equally to this work. The funding of the research is provided by the Innovation and Technology Support Programme (ITSP) from the Innovation and Technology Commission of HKSAR (Project ITS/175/23), the Innovation and Technology Commission of HKSAR through Hong Kong. Branch of National Precious Metals Material Engineering Research Centre, the City University of Hong Kong (Project 9667207). JLFS – RGC-Joint Laboratory Funding Scheme IMR-CityU Joint Laboratory of Nanomaterials & Nanomechanics (9070005 JLFS/E-102/24). Research Grants Council-Strategic Topics Grant (Project STG2/P-705/24-R). Guangdong Province Science and Technology Plan Project 2023B1212120008. Yunnan Precious Metals Laboratory Co., Ltd.

## Conflict of Interest

The authors declare no conflict of interest.

## Author Contributions

Y.Y.L. and J.L. were responsible for conceptualization and funding acquisition. Y.L., Z.M., B.L., and X.H. contributed to the methodology. X.T., Y.L., J.-H.L., H.L., and H.Y. conducted the investigation. and W.O., J.C.Y.H., J.L., and Y.Y.L. were involved in manuscript drafting and revision.

## Data Availability Statement

The data that support the findings of this study are available from the corresponding author upon reasonable request.

## Keywords

amorphous structures, nanocomposites, platinum-group metals, solar-driven desalination

Received: August 13, 2025
Revised: September 4, 2025
Published online:

[1] P. Zhang, H. Wang, J. Wang, Z. Ji, L. Qu, *Adv. Mater.* **2024**, *36*, 2303976.
[2] C. Dang, Y. Cao, H. Nie, W. Lang, J. Zhang, G. Xu, M. Zhu, *Nat. Water* **2024**, *2*, 115.
[3] B. Xu, M. Ganesan, R. K. Devi, X. Ruan, W. Chen, C. C. Lin, H. T. Chang, E. Lizundia, A. K. An, S. K. Ravi, *Adv. Mater.* **2025**, *37*, 2406666.
[4] Z. Mao, Y. Yao, J. Shen, J. Liu, Y. Chen, B. Zhou, Y. Chen, Q. Wang, J. Lu, *Nat. Water* **2024**, *2*, 93.
[5] Z. Mao, Q. Wang, Z. Yu, A. Osman, Y. Yao, Y. Su, H. Yang, J. Lu, *ACS Nano* **2024**, *18*, 22648.
[6] H. Yang, D. Li, X. Zheng, J. Zuo, B. Zhao, D. Li, J. Zhang, Z. Liang, J. Jin, S. Ju, *Adv. Mater.* **2023**, *35*, 2304699.
[7] Y. Liu, S. Pan, W. Xia, P. Qin, W. Wang, Q. Liu, X. Chen, L. Ma, S. Ding, Q. Wang, *Sci. Adv.* **2025**, *11*, adt2884.
[8] P. Cheng, H. Wang, H. Wang, D. Wang, P. A. van Aken, P. Schaaf, *Small* **2024**, *20*, 2400588.
[9] Y. Wang, Y. Ji, Y. Yang, Z. Chen, H. Sun, X. Wang, Z. Zou, H. Huang, *ACS Energy Lett.* **2024**, *9*, 336.
[10] Y.-G. Wu, C.-H. Xue, X.-J. Guo, M.-C. Huang, H.-D. Wang, C.-Q. Ma, X. Wang, Z.-Y. Shao, *Chem. Eng. J.* **2023**, *471*, 144313.
[11] Y. Li, Y. Shi, H. Wang, T. Liu, X. Zheng, S. Gao, J. Lu, *Carbon Energy* **2023**, *5*, 331.
[12] Z. Mao, Y. Han, J. Shen, L. Zhang, Y. Xie, J. Liu, H. Wu, Z. Yu, X. Duan, Y. Zhang, *Adv. Sci.* **2024**, *11*, 2405639.
[13] X. Zhao, X. Meng, H. Zou, Z. Wang, Y. Du, Y. Shao, J. Qi, J. Qiu, *Adv. Funct. Mater.* **2023**, *33*, 2209207.
[14] R. Zheng, T. Lin, W.-L. Zhao, R. Yin, H. Li, Z. Deng, W. Chen, Y.-F. Song, *Chem. Eng. J.* **2023**, *470*, 144103.

[15] H. Liu, F. Wu, X.-Y. Liu, J. Yu, Y.-T. Liu, B. Ding, *Nano Lett.* **2023**, *23*, 11907.
[16] D. Li, Z. Liang, H. Yang, M. Zhang, K. Cao, B. Zhao, Y. Wang, M. Peng, Y. Sun, L. Jiang, *Adv. Funct. Mater.* **2023**, *33*, 2300353.
[17] P. Cheng, M. Klingenhof, H. Honig, L. Zhang, P. Strasser, P. Schaaf, D. Lei, D. Wang, *Adv. Mater.* **2025**, *37*, 2415655.
[18] Y. Chen, Z. Mao, J. Yin, J. Shen, W. Ou, J. Lu, *Sep. Purif. Technol.* **2023**, *325*, 124637.
[19] H. S. Kang, J. W. Zou, Y. Liu, L. Ma, J. R. Feng, Z. Y. Yu, X. B. Chen, S. J. Ding, L. Zhou, Q. Q. Wang, *Adv. Funct. Mater.* **2023**, *33*, 2303911.
[20] E. Guénin, A. Fromain, A. Serrano, G. Gropplero, Y. Lalatonne, A. Espinosa, C. Wilhelm, *Commun. Mater.* **2023**, *4*, 84.
[21] H. Zhang, L. Zhang, H. Zhong, S. Niu, C. Ding, S. Lv, *Chem. Eng. J.* **2022**, *430*, 132675.
[22] J. Yang, S. Lv, J. Zuo, J. Wang, D. Wei, *Adv. Sustain. Syst.* **2025**, *9*, 2400330.
[23] J. Jiao, D. Chen, H. Zhao, Y. Dong, S. Mu, *Sci. China:Chem.* **2024**, *68*, 2217.
[24] J. Chen, M. Qi, Y. Yang, X. Xiao, Y. Li, H. Jin, Y. Wang, *Angew. Chem., Int. Ed.* **2025**, *137*, 202420860.
[25] H. Li, B. Zhu, J. Sun, H. Gong, J. Yu, L. Zhang, *J. Colloid Interface Sci.* **2024**, *654*, 1010.
[26] L. O. Paulista, A. F. Ferreira, B. Castanheira, M. B. Đolić, R. J. Martins, R. A. Boaventura, V. J. Vilar, T. F. Silva, *Appl. Catal. B-Environ.* **2024**, *340*, 123232.
[27] S. Biswas, A. Morag, N. Shauloff, N. Maman, R. Jelinek, *J. Mater. Chem. A.* **2024**, *12*, 20887.
[28] M. Kumar, K. K. Kar, P. Paik, *Chem. Eng. J.* **2024**, *499*, 156414.
[29] Y. Liu, Y. Chen, Y. Gong, H. Yang, J. Liu, *ACS Appl. Nano Mater.* **2023**, *6*, 5384.
[30] H. Zhou, Y. Gong, Y. Liu, A. Huang, X. Zhu, J. Liu, G. Yuan, L. Zhang, J.-a. Wei, J. Liu, *Biomaterials* **2020**, *237*, 119822.
[31] P. Li, Z. Chen, F. Xia, N. Wang, J. Zhao, X. Hu, M. Zhu, S. Yu, D. Ling, F. Li, *Adv. Healthcare Mater.* **2023**, *12*, 2302111.
[32] X. Chen, N. Yang, Y. Wang, H. He, J. Wang, J. Wan, H. Jiang, B. Xu, L. Wang, R. Yu, *Adv. Mater.* **2022**, *34*, 2107400.
[33] H. Wu, H. Wang, Y. Lv, Y. Wu, Y. Wang, Q. Luo, Y. Hui, L. Liu, M. Zhang, K. Hou, *Angew. Chem., Int. Ed.* **2025**, *64*, 202420306.
[34] Y. Zhang, Z. Wang, L. Wang, L. Zong, *Small* **2024**, *20*, 2400892.
[35] J. Xu, M. Song, Z. Fang, L. Zheng, X. Huang, K. Liu, *J. Controlled Release* **2023**, *353*, 699.
[36] D. Zhang, K. X. Teng, L. Zhao, L. Y. Niu, Q. Z. Yang, *Adv. Mater.* **2023**, *35*, 2209789.
[37] J. Chen, S. Yao, B. Wang, Q. Yu, B. Xue, P. Yin, *Angew. Chem., Int. Ed.* **2025**, *137*, 202416759.
[38] J.-Y. Jeong, J. M. Lee, Y. S. Park, S. Jin, S.-W. Myeong, S. Heo, H. Lee, J. G. Albers, Y.-W. Choi, M. H. Seo, *Appl. Catal. B: Environ.* **2024**, *356*, 124220.
[39] M. Zhu, Y. Li, F. Chen, X. Zhu, J. Dai, Y. Li, Z. Yang, X. Yan, J. Song, Y. Wang, *Adv. Energy Mater.* **2018**, *8*, 1701028.
[40] X. Tang, Y.-T. Cheng, J. Shen, J.-H. Liu, Z. Zhang, Z. Deng, F. Lyu, Y. Yang, G. Zhu, Z. Xu, *Adv. Eng. Mater.* **2023**, *25*, 2300430.
[41] J.-h. Liu, C. Huang, H. Wu, Y. Long, X. Tang, H. Li, J. Shen, B. Zhou, Y. Zhang, Z. Xu, *Sci. Adv.* **2024**, *10*, adk5047.
[42] T. P. Luxton, M. J. Eick, K. G. Scheckel, *J. Colloid Interface Sci.* **2011**, *359*, 30.
[43] C. Yang, K. Lin, J. Chang, *Ceram. Int.* **2015**, *41*, 11153.
[44] E. Santillán-Urquiza, F. Arteaga-Cardona, E. Hernandez-Herman, P. Pacheco-García, R. González-Rodríguez, J. Coffer, M. Mendoza-Alvarez, J. Vélez-Ruiz, M. Méndez-Rojas, *J. Colloid Interface Sci.* **2015**, *460*, 339.
[45] T. Ban, K. Inukai, T. Hattori, T. Nagata, C. Takai-Yamashita, Y. Ohya, *J. Sol-Gel Sci. Technol.* **2022**, *104*, 536.
[46] H. Wang, X. Li, Q. Ruan, J. Tang, *Nanoscale* **2020**, *12*, 12329.
[47] D. Chen, R. Yu, K. Yu, R. Lu, H. Zhao, J. Jiao, Y. Yao, J. Zhu, J. Wu, S. Mu, *Nat. Commun.* **2024**, *15*, 3928.
[48] B. Wu, X. Liu, P. Liu, G. Wu, L. Tian, X. Han, J. Li, X. Hong, *Nat. Synth.* **2025**, *4*, 370.
[49] G. Chen, R. Lu, C. Ma, X. Zhang, Z. Wang, Y. Xiong, Y. Han, *Angew. Chem., Int. Ed.* **2024**, *63*, 202411603.
[50] D. A. McKeown, P. L. Hagans, L. P. Carette, A. E. Russell, K. E. Swider, D. R. Rolison, *J. Phys. Chem. B.* **1999**, *103*, 4825.
[51] Y. Li, Y. Liao, J. Zhang, E. Huang, L. Ji, Z. Zhang, R. Zhao, Z. Zhang, B. Yang, Y. Zhang, *Angew. Chem., Int. Ed.* **2021**, *60*, 27113.
[52] B. Yang, Z. Zhang, P. Liu, X. Fu, J. Wang, Y. Cao, R. Tang, X. Du, W. Chen, S. Li, *Nature* **2023**, *622*, 499.
[53] J. Qiu, X. Xu, Z. Li, Y. Hu, G. Liu, X. Lv, J. Xu, B. Lu, *Nano Energy* **2024**, *130*, 110057.
[54] Y. Zhang, S. K. Ravi, S. C. Tan, *Nano Energy* **2019**, *65*, 104006.
[55] X. Xu, J. Qiu, Z. Li, A. Fu, S. Yuan, H. Li, B. Lu, *Desalination* **2025**, *611*, 118920.
[56] Y. Wang, W. Zhao, Z. Peng, Y. Feng, J. Lu, Y. Song, W. Xu, X. Wen, Z. Chen, Z. Wang, *Adv. Mater.* **2025**, 2502134.
[57] R. Li, M. Wu, H. Ma, Y. Zhu, H. Zhang, Q. Chen, C. Zhang, Y. Wei, *Adv. Mater.* **2024**, *36*, 2402016.
[58] L. Cui, C. Ma, P. Wang, H. Che, H. Xu, Y. Ao, *Appl. Catal. B-Environ.* **2023**, *337*, 122988.
[59] Y. Zhang, Y. Wang, B. Yu, K. Yin, Z. Zhang, *Adv. Mater.* **2022**, *34*, 2200108.
[60] B. Yu, Y. Wang, Y. Zhang, Z. Zhang, *Nano Res.* **2023**, *16*, 5610.
[61] Y. Liu, Z. Liu, Q. Huang, X. Liang, X. Zhou, H. Fu, Q. Wu, J. Zhang, W. Xie, *J. Mater. Chem. A.* **2019**, *7*, 2581.
[62] L. Zhou, S. Zhuang, C. He, Y. Tan, Z. Wang, J. Zhu, *Nano Energy* **2017**, *32*, 195.
[63] Q. Zhang, L. Li, B. Jiang, H. Zhang, N. He, S. Yang, D. Tang, Y. Song, *ACS Appl. Mater. Interfaces.* **2020**, *12*, 28179.
[64] R. Cui, J. Wei, C. Du, S. Sun, C. Zhou, H. Xue, S. Yang, *J. Mater. Chem. A.* **2020**, *8*, 13311.
[65] Z. Huang, S. Li, X. Cui, Y. Wan, Y. Xiao, S. Tian, H. Wang, X. Li, Q. Zhao, C.-S. Lee, *J. Mater. Chem. A.* **2020**, *8*, 10742.
[66] Y. Zhang, B. Yu, Y. Shi, F. Tan, Z. Zhang, *Small* **2024**, *20*, 2310725.
[67] X. Geng, D. Zhang, Z. Zheng, G. Ye, S. Li, H. Tu, Y. Wan, P. Yang, *Nano Energy* **2021**, *82*, 105700.